

Acoustic band engineering in terahertz quantum-cascade lasers and arbitrary superlattices

Aleksandar Demić ^{*}, Alexander Valavanis , Paul Dean , Lianhe Li , A. Giles Davies,
Edmund H. Linfield, and John Cunningham
School of Electronic and Electrical Engineering, University of Leeds, Leeds LS2 9JT, United Kingdom

James Bailey , Andrey Akimov , and Anthony Kent 
School of Physics and Astronomy, University of Nottingham, Nottingham NG7 2RD, United Kingdom

Paul Harrison 
School of Computing and Engineering, University of Huddersfield, Huddersfield HD1 3DH, United Kingdom

 (Received 17 March 2023; revised 17 May 2023; accepted 19 May 2023; published 14 June 2023)

We present theoretical methods for the analysis of acoustic phonon modes in superlattice structures, and terahertz-frequency quantum-cascade lasers (THz QCLs). Our generalized numerical solution of the acoustic-wave equation provides good agreement with experimental pump-probe measurements of the acoustic resonances in a THz QCL. We predict that the detailed layer structure in THz QCLs imprints up to ~ 2 GHz detuning of the acoustic mode spacing, which cannot be seen in analytical models. This effect is strongest in devices with large and abrupt acoustic mismatch between layers. We use an acoustic deformation potential within a density-matrix approach to analyze electron transport induced in a range of the most common THz QCL active-region design schemes. We conclude that acoustic modes up to ~ 200 GHz are capable of significantly perturbing QCL transport, highlighting their potential for ultrafast modulation of laser emission.

DOI: [10.1103/PhysRevB.107.235411](https://doi.org/10.1103/PhysRevB.107.235411)

I. INTRODUCTION

Superlattices consist of periodic layer sequences of two or more materials. Acoustic waves (or phonons) within such structures are perturbed by the variation in acoustic impedance between the materials, causing their dispersion to differ from that of a bulk material. Furthermore, the periodicity of the structure folds the acoustic-wave dispersion into a Brillouin zone [1,2], characterized by a set of acoustic stopbands (or eigenmodes).

Vibrational dynamics in superlattices has been studied experimentally using Raman scattering techniques [2–6] and femtosecond pump-probe techniques, where typically longitudinal acoustic (LA) modes [7,8] or (more recently) transverse acoustic (TA) modes [9,10] have been explored. Recent investigations have also demonstrated the potential for acoustic waves in the ~ 100 GHz range to modulate electron transport and tunneling [11–13].

Terahertz-frequency quantum-cascade lasers (THz QCLs) [14] are a specific case of interest, in which coherent THz photons are generated using electronic intersubband transitions within a complex multilayered superlattice. The picosecond electronic lifetimes in THz QCLs potentially enable ultrafast

light modulation [15] required for frequency comb generation [16], active mode locking [17], amplitude, frequency [18], and phase stabilization [19]. THz QCLs thus show potential for applications in metrology [20], high-resolution spectroscopy [21,22], and ultrafast wireless communications [23].

The most common THz QCL modulation techniques, however, are limited to relatively low bandwidths. For example, direct gain modulation through the applied voltage is, in practice, limited to $\lesssim 35$ GHz due to parasitic inductance [24,25]. Other approaches exploit the possibility of controlling effective cavity losses [26,27], but they are also limited due to parasitic effects within the modulating elements.

In previous work [28], we explored the potential to overcome these limits through ultrafast modulation of THz QCLs using bulk acoustic waves. Although acoustic phonons have a weaker effect than optical phonons on electron transport in THz QCLs, externally generated acoustic pulses can exploit the picosecond-scale dynamics of strain propagation through the device. However, the complex layer structure within a THz QCL active region perturbs the acoustic velocity across the superlattice structure. As such, it is inaccurate to consider the phonons as having bulklike dispersion, or even that of a simple Kronig-Penney superlattice. There is also a range of different design schemes for THz QCLs, with varying electronic transport behavior [29], and it is unclear which scheme is most susceptible to acoustic modulation. It is therefore important to develop a detailed and accurate understanding of acoustic phonon dispersion within a QCL and their effect on electron transport in order to explore and ultimately optimize this effect.

^{*}A.Demic@leeds.ac.uk

We have therefore developed an “envelope function”-like model to study acoustic phonon modes in *arbitrary* semiconductor heterostructures. Although transfer-matrix methods are widely used to find the eigenmodes of wavelike functions in simple structures with well-defined layers, they scale poorly to larger or more complex structures, and they are unsuitable for systems with diffuse interfaces. We therefore use a finite-difference discretization scheme to analyze the acoustic modes in superlattices with arbitrary interface geometries. We couple the acoustic perturbation to the strain in a density-matrix model for electron transport in a THz QCL, and we use this to analyze the strength of the acoustic modulation effect in a range of QCL design schemes.

In Sec. II we present our theoretical model for acoustic phonon modes in arbitrary heterostructures, and in Sec. III we validate this against experimental pump-probe measurements of a THz QCL structure [28]. In Sec. IV, we use the model to simulate and analyze the acoustic phonon mode structure in three exemplar THz QCL active region designs, along with several superlattice structures with diffuse layer profiles. We demonstrate the advantages of using a finite-difference eigenvalue calculation compared with a more commonly used transfer-matrix approach [8]. We also demonstrate that the acoustic mode frequencies in THz QCLs are aperiodic, as a result of the complex multilayer heterostructures used in their active regions. In Sec. V, we consider the effect of acoustic phonon modes on electron transport in THz QCLs by employing a density matrix transport model [30,31]. We discuss the prospects for acoustic modulation of THz emission from QCLs, and we predict the QCL design schemes that would be most susceptible to the effect.

II. ENVELOPE-FUNCTION MODEL OF ACOUSTIC PHONON MODES IN ARBITRARY HETEROSTRUCTURES

The starting point for our model is the acoustic wave equation [32]:

$$\frac{\partial}{\partial z} v_s^2(z) \frac{\partial}{\partial z} p(z, t) - \frac{\partial^2}{\partial t^2} p(z, t) = 0, \quad (1)$$

where the acoustic-wave pressure $p(z, t)$ depends on position z (in the growth direction) and time t . Here, $v_s(z)$ is the acoustic velocity, which, due to variation of heterostructure materials, has a z -dependent profile.

This equation can be solved using a variable separation method (Fourier method), closely resembling the envelope-function approach, which is commonly employed for solving the Schrödinger equation. If we assume $p(z, t) = p_0 \psi(z) \exp(-i\omega t)$, where p_0 is the wave amplitude, ω is the angular frequency, and $\psi(z)$ is the envelope of the acoustic wave, Eq. (1) folds into

$$-\frac{\partial}{\partial z} v_s^2(z) \frac{\partial}{\partial z} \psi(z) = \omega^2 \psi(z). \quad (2)$$

Analytical solutions of Eq. (2) are possible for an ideal acoustic cavity of length d , consisting of a homogeneous bulk medium with $v_s(z) = v_{\text{bulk}}$, surrounded by impenetrable reflective surfaces, such that $\psi(0) = \psi(d) = 0$. By assuming a plane-wave form of the normalized acoustic wave function, $\psi(z) = \exp(iqz)$, standing-wave solutions to Eq. (2) are

found, with equidistant wave vectors, $q_n = n\pi/d$, and corresponding frequencies:

$$\omega_{\text{bulk},n} = \frac{n\pi v_{\text{bulk}}}{d}, \quad (3)$$

where n is an integer representing the phonon mode index.

For periodic superlattice structures, the phonon mode is no longer confined to specific wave vectors. For a period length d_{sl} , the normalized acoustic wave functions take a Bloch form, such that $\psi_q(z) = u_q(z) \exp(iqz)$. This consists of an envelope function, with the same periodicity as the superlattice, $u_q(z + d_{\text{sl}}) = u_q(z)$, multiplied by a plane-wave $\exp(iqz)$, with arbitrary wave vector q . The latter can be understood as a steady rotation in the complex plane, as the wave function extends across the length of the structure.

The periodic nature of the structure allows the phonon dispersion to be folded into the first Brillouin zone such that $|q| \leq q_B$, where $q_B = \pi/d_{\text{sl}}$. Two sets of symmetry points can be defined within this zone: Brillouin zone center (BZC) modes with $q = 0$, and Brillouin zone edge (BZE) modes with $q = \pi/d_{\text{sl}}$, and they represent cases in which $\psi(z) = \pm \psi(z + d_{\text{sl}})$. It is important to note that the BZC and BZE wave vectors are identical to those for standing waves in an ideal cavity of length $d = d_{\text{sl}}$. Indeed, it is a fundamental result of the Bloch model that the eigenmodes of an isolated unit cell of a periodic system provide a close approximation to the BZE and BZC solutions for a periodic structure [32]. It is, therefore, desirable to find a computationally efficient means of computing the single-period eigenmodes. There are some limitations to this single-period approach: only the BZC/BZE standing-wave solutions can be computed, and the width of the frequency stopband around these points cannot be determined. Although a more generalized periodic solver would be required to overcome these limitations, our approach allows rapid and direct computation of the solutions, and it can be applied to arbitrary heterostructures including those with poorly defined interfaces.

Equation (2) can be discretized using a finite-difference approximation by defining samples of the wave function and acoustic velocity at evenly spaced points i along the z direction:

$$a_i \psi_{i-1} + b_i \psi_i + c_i \psi_{i+1} = \omega^2 \psi_i, \quad (4)$$

where

$$a_i = -\frac{v_{i-1}^2 + v_i^2}{2\delta z^2}, \quad (5)$$

$$b_i = \frac{v_{i-1}^2 + 2v_i^2 + v_{i+1}^2}{2\delta z^2}, \quad (6)$$

$$c_i = -\frac{v_{i+1}^2 + v_i^2}{2\delta z^2}. \quad (7)$$

The half-integer samples of squared velocity that typically arise in central finite differences [32] are taken as the spatial average of neighboring points. It may now be solved by rewriting it as a tridiagonal matrix equation:

$$\mathbf{H}\psi = \omega^2 \psi, \quad (8)$$

where

$$\mathbf{H} = \begin{pmatrix} b_1 & c_1 & 0 & \cdots & 0 \\ a_1 & b_2 & c_2 & \cdots & 0 \\ 0 & \ddots & \ddots & \ddots & 0 \\ \vdots & \cdots & a_{N-2} & b_{N-1} & c_{N-1} \\ 0 & \cdots & 0 & a_{N-1} & b_N \end{pmatrix}. \quad (9)$$

The eigenvectors of the \mathbf{H} matrix give the envelopes of the acoustic wave $\psi(z)$ for each mode, and the corresponding eigenvalues give the square of the angular frequency ω .

This solution approach provides several advantages over commonly applied layer-by-layer transfer-matrix methods [8]. All eigenvalues are computed simultaneously to machine precision, requiring instead a separate root-finding process for each mode. The numerical precision of the obtained eigenvalues can therefore be increased in a straightforward way by increasing the spatial mesh density. The most significant advantage, though, is that *arbitrary* heterostructure profiles may be considered, including diffuse structures, in which layers are not separated by abrupt interfaces, without any increase in computational expense.

Our model can thus be applied directly to complex periodic heterostructures such as GaAs/Al_xGa_{1-x}As THz QCL gain media (where typically $x = 0.1-0.3$). Although the acoustic velocity varies only by $\lesssim 5\%$ between the layers in typical structures, this represents a potentially very large margin of error for the design of high-precision radiofrequency modulators and transducers. As such, it is instructive to compare the numerical results of our model to analytical solutions for a bulk medium of identical length.

An improvement to the homogeneous-material model can be obtained by taking a reciprocal average of the ratios between the total length d_l and acoustic velocity v_l in each layer l of the structure [8]:

$$\omega_{\text{avg},n} = \frac{n\pi}{\sum_l \frac{d_l}{v_l}} \quad \text{or} \quad \frac{1}{\omega_{\text{avg},n}} = \sum_l \frac{1}{\omega_l}, \quad \omega_l = \frac{n\pi v_l}{d_l},$$

$$\omega_{\text{avg},n} = n\pi \left(\frac{d_{\text{well}}}{v_{\text{well}}} + \frac{d_{\text{barrier}}}{v_{\text{barrier}}} \right)^{-1}. \quad (10)$$

Here, ω_l can be interpreted as the resonant frequency of each isolated layer. The latter simplified expression denotes the most common case, in which the superlattice contains only two materials (i.e., alternating well and barrier layers). In this work, we have used $v_{\text{bulk}} = 4710 \text{ ms}^{-1}$, $v_{\text{AlAs}} = 5650 \text{ ms}^{-1}$, while the acoustic velocity in an arbitrary Al_xGa_{1-x}As barrier alloy was evaluated through linear interpolation as $v_{\text{barrier}} = v_{\text{bulk}} + x(v_{\text{AlAs}} - v_{\text{bulk}}) \text{ ms}^{-1}$.

Equations (3) and (10) provide simple approximations to the exact solution of Eq. (2), in which the spatial variation of acoustic velocity is ignored. We define the frequency deviations of these approximate solutions from the exact numerical values f_n as

$$\Delta f_{\text{bulk},n} = f_n - \frac{nv_{\text{bulk}}}{2d_{\text{sl}}},$$

$$\Delta f_{\text{avg},n} = f_n - \frac{n}{2\sum_l \frac{d_l}{v_l}}. \quad (11)$$

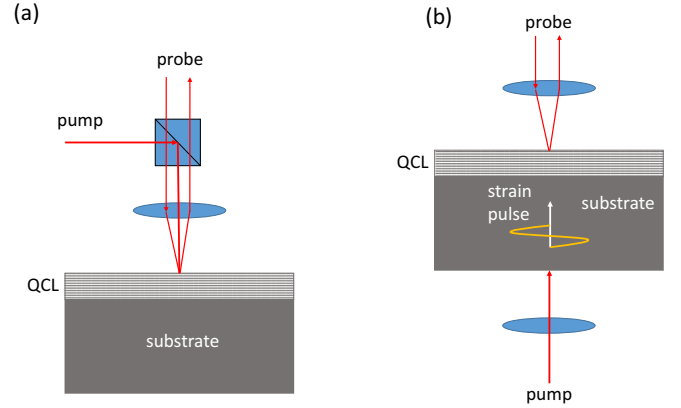


FIG. 1. Schematic illustrations of ASOPS experimental configurations, showing (a) reflection mode, and (b) transmission mode geometries.

These deviations allow us to determine the extent to which the detailed superlattice layer structure affects the phonon modes, and to investigate the prospect of phononic band-structure engineering. It is important to note that the model in Eq. (2) implicitly assumes linear dispersion of the acoustic phonon branch, which may not be valid for modes with high index n , unless a frequency-dependent correction is introduced in v_s . Experimental work [10] typically reports modes up to 1 THz, with higher modes lost to dispersion. For this reason, we will limit analysis to the first 100 modes since this accounts for frequencies up to 1 THz for most cases of interest in the following sections.

III. PUMP-PROBE CHARACTERIZATION OF 2.8-THz QCL GAIN MEDIA

To validate our arbitrary-heterostructure model, we compare its predictions with experimental measurements of phonon modes in a complex THz QCL heterostructure we have previously used for time-domain acoustic modulation studies [28]. This QCL comprises 88 periods of a GaAs/Al_{0.14}Ga_{0.86}As nine-well “hybrid” band-structure design and lases around 2.8 THz [33]. The 13.9- μm -thick QCL active region was grown using molecular-beam epitaxy on a 150- μm -thick semi-insulating GaAs substrate, as described in [28].

Here, we present experimental measurements of the phonon modes in the QCL gain media using asynchronous optical sampling (ASOPS) femtosecond optical pump-probe techniques. An unprocessed sample of the same epitaxially grown wafer as in [28] was used in this study (i.e., without a ridge-waveguide or electrical contact deposition). A 50-nm-thick aluminum film was deposited on the bottom surface of a section of semiconductor wafer (the substrate), to act as an acoustic transducer.

Two ASOPS measurement schemes, shown in Fig. 1, were used. In each of these, a femtosecond pump laser is used to generate acoustic waves within the semiconductor sample. A delayed probe-laser pulse is then used to measure small changes over time in the reflectivity of the sample surface, $\Delta R/R$, resulting from the strain wave propagating through the

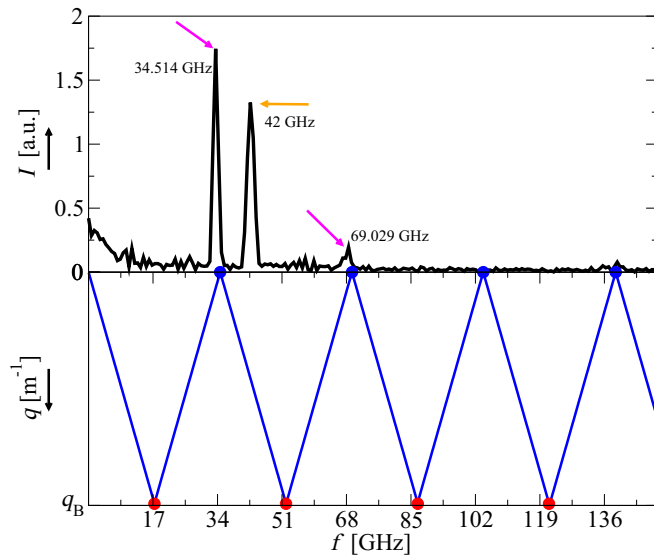


FIG. 2. Experimental probe reflectivity spectrum (top), obtained using a reflection-mode ASOPS geometry, and folded dispersion of the first Brillouin zone (bottom), obtained by solving Eq. (2) for a single period of the QCL. Blue and red circles indicate BZC and BZE modes, respectively.

sample. The Fourier transform of the resulting temporal trace then gives the spectrum of phonon modes.

In the scheme in Fig. 1(a), the top of the epitaxial QCL active region stack was pumped directly with $\lambda = 810$ nm pulses with a fluence of 0.6 mJ cm^{-2} , and with the sample at room temperature. It was probed on the same surface with $\lambda = 810$ nm pulses with a fluence of $20 \mu\text{J cm}^{-2}$. In this configuration, absorption of the pump light excites coherent phonons with wave vectors corresponding to the periodicity of the QCL structure (i.e., the $q = 0$ modes in the folded dispersion). These modes do not strictly satisfy the selection rules for detection by the probe laser (i.e., $q = 2k_L$, where k_L is the photon wave vector of the optical probe). However, due to the finite absorption length of the probe light in the structure and the bandwidth of the laser pulses, the excited $q = 0$ modes become observable in this scheme [34].

The top panel in Fig. 2 shows the experimental reflectivity spectrum obtained using an offset of 800 Hz between the pump and probe laser repetition rates. This provided measurements of the wafer reflectivity at intervals of 640 fs, over a total 1282 ns sampling window, giving a spectral resolution of 780 MHz. Phonon modes are observed in the resulting spectrum at 35, 42, and 69 GHz.

For comparison, the bottom panel shows the approximate folded dispersion relation, which was calculated using the BZC and BZE modes obtained by solving Eq. (2) for a single period of the QCL structure. The calculated modes (to 1 s.f. precision) were 17.4, **34.7**, 52.1, **69.5**, 86.8, **104**, 121, **139**, 156, **174**, and 191 GHz, where only the BZC modes (highlighted in bold) are detectable in this scheme. The pink arrows in Fig. 2 are therefore identifiable (to within 1 GHz) as the first two BZC modes of the heterostructure. The orange arrow in Fig. 2 indicates a mode at 42 GHz, which does not correspond to any calculated BZE/BZC modes of the heterostructure.

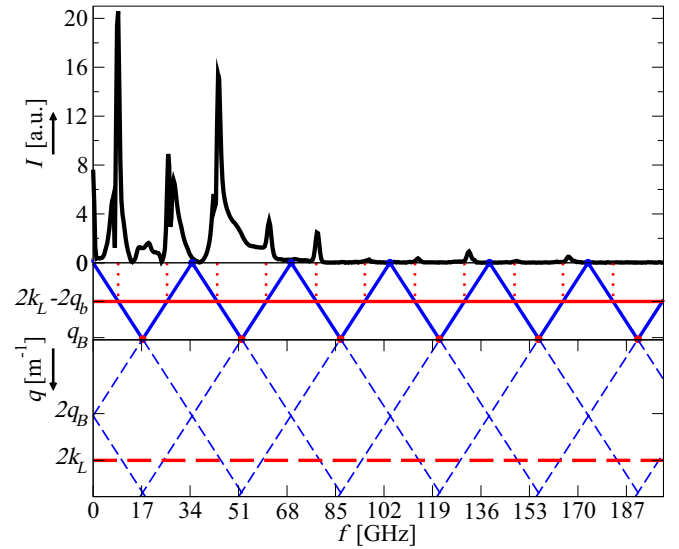


FIG. 3. Experimental probe reflectivity spectrum (top), using the configuration in Fig. 1(b), and acoustic dispersion resulting from the model in Eq. (2). Solid blue lines represent the phonon dispersion, folded into the first Brillouin zone, while dashed lines represent the extended dispersion at higher phonon wave vectors. The red dashed line corresponds to $q = 2k_L$, and the red solid line shows this folded into the first phonon Brillouin zone.

Instead, this is identifiable as a result of Brillouin scattering, i.e., interference between reflections of the probe pulse from the surface and from a strain pulse within the sample, with a frequency given by $2nv_s/\lambda = 42$ GHz, where $n = 3.68$ is the refractive index of the medium.

In the second scheme, shown in Fig. 1(b), the QCL structure was pumped indirectly, using broadband picosecond-duration acoustic strain pulses. These were generated by absorbing a $\lambda = 800$ nm pulse in a ~ 50 -nm-thick Al film on the opposite side of the GaAs substrate to which the QCL structure was grown. The sample was cooled in a helium cryostat to 10 K, so that the substrate was transparent to the high-frequency phonons in the pulse. The strain pulses are bipolar in form with approximately 20 ps duration, and the corresponding broad-bandwidth phonon spectrum is peaked at about 50 GHz [35]. When the strain pulse enters the QCL structure, it is able to excite *any* phonon mode within the bandwidth of the pulse (i.e., not only the $q = 0$ modes).

As in the first scheme, the phonons in the QCL structure were detected through changes in the reflected probe intensity. In this case, however, phonon modes that satisfy the selection rule, $q = 2k_L = 4\pi n/\lambda$, are detected by the probe, and they are the most prominent in the measured spectrum. For this reason, the probe wavelength $\lambda = 810$ nm influences the detected mode frequencies. Since the probe wave vector lies outside the first acoustic Brillouin zone ($2k_L > q_B$), the selection rule may be folded into the zone such that $q = 2k_L - 2q_B$, which is graphically illustrated by horizontal red lines in Fig. 3. The modes that are detected by this scheme thus correspond to intersections between the acoustic dispersion $q(f)$ and the red line at $2k_L - 2q_B$. As our model detects the BZC/BZE modes of the superlattice, the simplest approximation for the dispersion relation is $q(f) = 2\pi|f - f_{2n}|/v_{\text{bulk}}$, where f_{2n}

correspond to the BZC modes, depicted by blue circles in Fig. 3,

$$f = f_{2n} \pm \left(\frac{v_{\text{bulk}} n_{\text{ref}}}{\lambda} - \frac{v_{\text{bulk}}}{d_{\text{sl}}} \right). \quad (12)$$

For the measurement in Fig. 3, the intersection points corresponding to Eq. (12) are $f = f_{2n} \pm 8.79$ (GHz). This yields predicted spectral peaks at 8.79, 25.9, 43.5, 60.7, 78.2, 95.3, 113, etc. The experimental data peaks in Fig. 3 are found at 9, 26, 44, 62, 79, 97, 114, etc., in good agreement with the theoretical predictions. The accurate prediction of acoustic eigenmodes in this structure gives confidence in the use of the model to analyze and predict such effect in wider range of heterostructures in the following sections.

We note that further improvement between predicted and measured peaks could be made in Eq. (12). The acoustic velocity for each even eigenmode can be evaluated better by using the eigenvector solutions of Eq. (2) as the orthonormal basis, in order to calculate the probable acoustic velocity of each mode as the expectation value $v_n = \langle \psi_n | v(z) | \psi_n \rangle$. Similarly, the refractive index of $n_{\text{ref}} = 3.68$ corresponds to the bulk value of GaAs, if a weighted average is taken, depending on the content of AlAs in the period, $n_{\text{ref}} = 3.64$, which changes Eq. (12) to predict sidebands around even modes as $f = f_{2n} \pm 8.33$ (GHz). We could also calculate the refractive index expectation value for each stopband as $n_{\text{ref}} = \langle \psi_n | n_{\text{ref}}(z) | \psi_n \rangle$. In [10] the authors accounted for the mismatch between measurement and theory by assuming a nominal layer thickness growth variation of $\sim 3\%$, however we note that numerical solutions of Eq. (2) provide significantly better precision than the bulk approximation for BZE and BZC modes. Detected data in Fig. 3 have a finite bandwidth around each detected mode, where the signal even has contributions around $q = q_B$ (the odd stopbands) which occur due to complex phonon-photon interactions and material fluctuations that are not considered in our model.

IV. ACOUSTIC BAND-STRUCTURE ENGINEERING

As the acoustic velocity mismatch is relatively small in practical GaAs/AlGaAs heterostructures, the BZE/BZC modes are approximately evenly spaced, as expected from Eq. (3). However, the heterostructure layer composition introduces some deviation from these approximate solutions, which could potentially allow more precise design of acoustic band structure. We predict that this deviation would be enhanced in heterostructures with greater variation of acoustic velocity between layers, for example in superlattices with a greater Al content in the barrier alloy. In this section, we explore this deviation for a range of superlattice structures, and we discuss the prospects for band-structure engineering.

A. THz QCL gain media

The resonant acoustic modes are approximately equidistant both numerically and experimentally for the “hybrid” THz QCL structure we considered in the previous section. QCL design schemes can, however, differ considerably in terms of period length and barrier alloy composition, which are key parameters in Eq. (10). We will therefore consider four

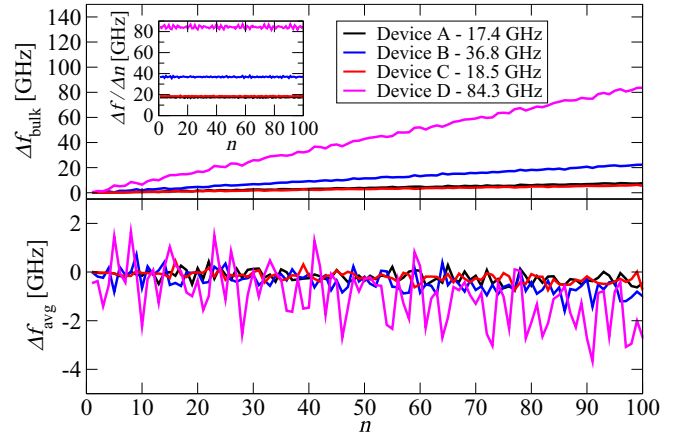


FIG. 4. Frequency offset from the bulk (top) and average (bottom) approximation calculated by Eq. (11) for QCL devices A–D. Inset: the frequency difference between consecutive resonant acoustic modes for the corresponding structures.

exemplar THz QCL structures with considerable variation in their layer composition, which are detailed in the Appendix:

(1) Device A: the hybrid QCL design discussed in the previous section, which employs a nine-well GaAs/Al_{0.14}Ga_{0.86}As heterostructure, of total 1362 Å period length [28].

(2) Device B: an LO-phonon depopulated design [10], which employs a three-well GaAs/Al_{0.15}Ga_{0.85}As design, of total 643 Å period length.

(3) Device C: a bound-to-continuum (BTC) design [30], which employs an eight-well GaAs/Al_{0.1}Ga_{0.9}As heterostructure, of total 1150 Å period length.

(4) Device D: an LO-phonon depopulated design with very high Al content in the barrier alloy [36], which employs a two-well, GaAs/Al_{0.3}Ga_{0.7}As design, of total 269.3 Å period length.

The inset in Fig. 4 shows the deviation between consecutive modes in each of these structures, as obtained from solving Eq. (2) numerically. The results for devices A and B are in good agreement with the mode spacing seen experimentally in Sec. III and in Ref. [10], respectively.

The top and bottom panels of the figure show the deviation between the exact numerical solution of Eq. (2) and the approximations for homogeneous media, as given in Eq. (11). The deviation from the homogeneous model is greatest for device D, and smallest for device C, due to the large acoustic-velocity mismatch between layers in the heterostructure. Device D also exhibits a periodic ($\Delta n \approx 10$) variation in the deviation from the analytical solutions, which we will separately examine later. In each case, the deviation from Eq. (3) increases approximately linearly with respect to the mode index, and it is largest for device D. However, the deviation from Eq. (10) remains approximately centered around zero for all mode indices. We can conclude that the bulk approximation in Eq. (3) underestimates the effective velocity of acoustic modes in a realistic heterostructure, and creates significantly larger offsets than the average-velocity approximation in Eq. (10), whose estimation provides < 2 GHz

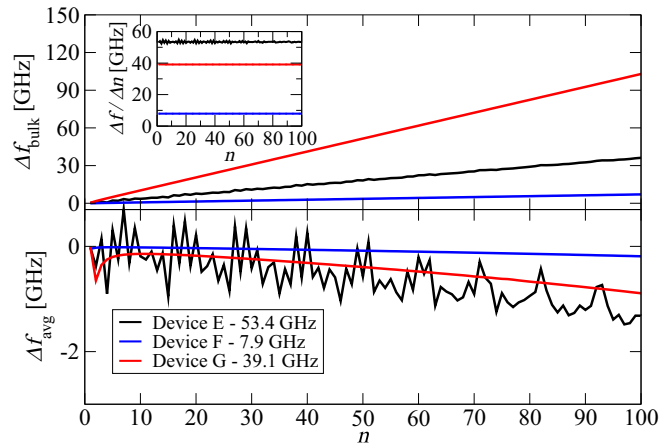


FIG. 5. Frequency offset from the bulk (top) and average (bottom) approximation calculated by Eq. (11) for variable barrier height LO phonon THz QCL structure [37] (device E), a parabolic quantum-well superlattice (device F) that quadratically varies Al content $x = 0-0.14$ across 3000 Å period length and a parabolic quantum well (device G) with varying Al content $x = 0-0.42$ across 620 Å well length. We used a monolayer step of 2.825 Å for generating the parabolic profiles. Inset: the frequency difference between consecutive resonant acoustic modes for the corresponding structures.

mismatch from numerical values even for structures with high barriers.

B. Superlattices with nonuniform layer profiles

One of the main advantages of the model in Eq. (2) is its ability to model arbitrary heterostructure profiles, such as those with poorly defined interfaces arising from interdiffusion or surface-segregation of alloy components during epitaxial growth. We therefore consider three exemplar superlattice structures with nonuniform layer compositions, and analyze their mode structure:

(1) Device E: A step-barrier LO-phonon depopulated THz QCL [37] that employs a three-well design with two different barrier heights in its period ($x = 0.15$ and 0.075) and has 444 Å period length.

(2) Device F: A wide parabolic quantum well GaAs/Al_cGa_{1-x}As superlattice [38] that varies $x = 0-0.14$ across 3000 Å period length.

(3) Device G: A narrow parabolic quantum well GaAs/Al_xGa_{1-x}As superlattice [39] that varies $x = 0-0.42$ across 620 Å period length.

Layer composition and functions that generate parabolic profiles can be found in the Appendix.

In Fig. 5 we present the results of our calculations on these structures. Device E is structurally similar to the THz QCL structures analyzed in Fig. 4, however it displays a more pronounced noislike variation between consecutive modes in Fig. 5, even though its highest barrier is $x = 0.15$ and we expected similar behavior to device B. It is likely that the additional perturbation in the heterostructure profile generates different resonance effects. By contrast, the parabolic quantum-well potentials in Fig. 5 are very well described by the average frequency formula in Eq. (10). This indicates that the fine structure of the acoustic dispersion is a result

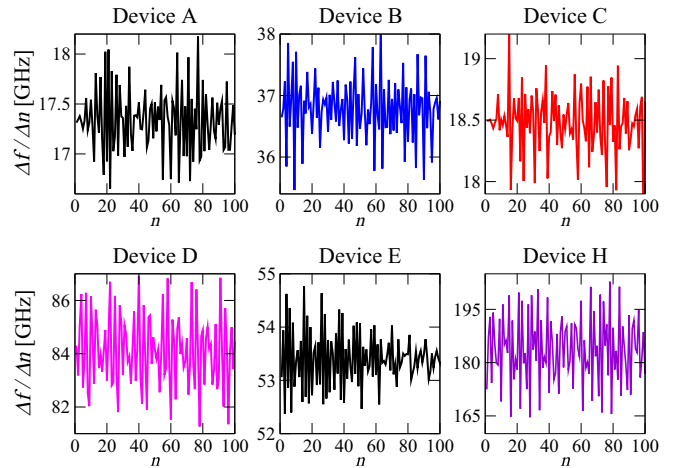


FIG. 6. The frequency difference between consecutive resonant acoustic modes for the corresponding structures analyzed in this section.

of interface mismatch within the heterostructure, and this is effectively damped by the use of diffuse interface geometry. The deviation is also larger in structures where there is a larger mismatch in barrier height. This may be of significant importance in material systems where there is a large mismatch between acoustic velocities in well and barrier material, or where the acoustic velocities are larger than in GaAs, which can also apply in midinfrared QCL designs.

C. High-precision frequency control

Our experimental and theoretical analysis in the previous sections has shown that the spacings between consecutive BZE and BZC modes in arbitrary superlattices are determined by two factors. First, the *average* spacing between modes is given to a reasonable level of accuracy by Eq. (10). This is determined solely by the length of the heterostructure period, and its average alloy composition. In other words, this “coarse” tuning of the acoustic dispersion results from the periodicity of the superlattice. The second, fine-tuning component results from the detailed layer structure of the superlattice, and is most prominent in systems with a large, and abrupt mismatch between the acoustic velocity in each layer. To confirm that this effect is not caused by numerical error, we used 20 000 spatial points for solving the eigenvalue problem in Eq. (2), and performed an error convergence check. In some cases, this fine-tuning component exhibits a periodicity, which we investigate further in this section, through simulation of the previous QCL devices (A–E). We have included an additional two-well GaAs/AlAs superlattice structure [8], denoted “device H” here, for which TA phonon spectra have previously been analyzed experimentally. For this TA-branch dispersion, $v_{\text{GaAs}} = 3329 \text{ ms}^{-1}$ and $v_{\text{AlAs}} = 3957 \text{ ms}^{-1}$ were assumed.

Figure 6 shows the calculated BZE/BZC modes for each of these devices. We observe that devices B, C, and H do not exhibit a well-defined periodicity, device D has a clear periodic envelope every 18 modes, device E has an attenuating envelope every ~ 11 modes, and device A has a weakly defined envelope every ~ 44 modes. We hypothesize that the observed periodicity is a consequence of an intraperiod resonance of the

acoustic wave with a layer within the superlattice. This is most likely to occur within an AlGaAs barrier layer, as the acoustic velocity is higher than in the well layers, meaning the modes are more likely to be confined in the barriers. For an observed period Δn in Fig. 6, we can estimate the suspected barrier layer width by assuming modes are equidistant through average approximation in Eq. (10) and apply the bulk-confinement approximation for that layer:

$$L_n \approx \frac{\Delta n \pi v_{\text{barrier}}}{\omega_{\text{avg}}}. \quad (13)$$

Interestingly, Eq. (13) is in good agreement with observations made in Fig. 6 as it provides a layer width equal to one of the dominant barriers in the corresponding designs.

(1) Device D has a very clear $\Delta n \approx 18$ envelope and $L_{18} = 16.44 \text{ \AA}$, which is close to the 17.5 \AA barrier width within this structure.

(2) Device E has an attenuating envelope with $\Delta n \approx 11$ envelope, and $L_{18} = 41.21 \text{ \AA}$, which is related to one of the three barriers of this structure (41, 43, and 46 \AA).

(3) Device H exhibits a Fourier transform peak at $\Delta n \approx 6$, and $L_6 = 18.65 \text{ \AA}$, which corresponds to the only two 17 \AA barriers within the structure.

(4) Device A has a weak $\Delta n \approx 44$ period, and $L_{44} = 31.66 \text{ \AA}$, which corresponds to multiple 31 \AA barriers within the structure.

The amplitude of variations in Fig. 6 can directly be affected by increasing barrier height and therefore the acoustic velocity in the barriers. To confirm our estimate in Eq. (13), we alter the layer structure of studied devices as follows (layer composition is presented in the Appendix):

(1) Device D₁: we double the thickness of the 17.5 \AA barrier in device D to confirm that the period of oscillations halves.

(2) Device C₁: we make the 24-\AA barrier the largest in device C by replacing its material with pure AlAs ($x = 1$).

(3) Device C₂: we set two very tall $x = 1$ barriers in device C, a 24 \AA layer as in C₁, and a 30 \AA layer to study the effect of having two dominant barriers in the design.

(4) Device I: we consider a GaAs/AlAs heterostructure with three 150 \AA wells separated by barriers of 20, 40, and 80 \AA . If the periodicity of the confinement is caused by the barrier layers, this will create an ideal periodicity matching condition.

(5) Device J: we consider a heterostructure with two sets of identical wells and fixed barrier width as shown in the Appendix. This should create a perfectly periodic structure that is independent of the barrier height. To confirm this, we use $x = 0.1$ in the barrier material.

The results, shown in Fig. 7, agree with our approximation in Eq. (13). Doubling the barrier width of device D reduced the periodicity to $\Delta n \approx 9$ in device D₁, which corresponds to $L_9^{\text{D}_1} = 34.82 \text{ \AA}$. Setting the 24 \AA barrier in device C to $x = 1$ has fully confined consecutive mode dependence for device C₁, yielding $L_{60}^{\text{C}_1} = 24.65 \text{ \AA}$. However, setting two very high barriers in C₂ results in a more complex mode structure, and the Fourier transform of the data reveals peaks that correspond to $L_{60}^{\text{C}_2} = 24.65 \text{ \AA}$ and $L_{46}^{\text{C}_2} = 32.15 \text{ \AA}$, in excellent agreement with the barriers whose heights were increased. This result provides us with a fundamental understanding that the com-

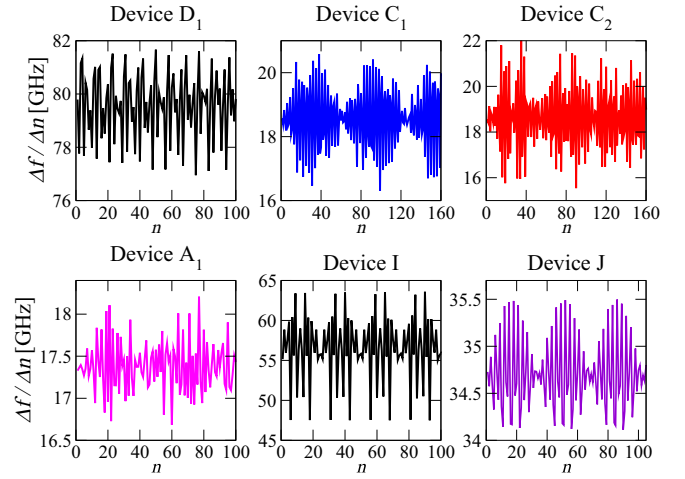


FIG. 7. The frequency difference between consecutive resonant acoustic modes for altered structures that test the validity of the approximation created by Eq. (13)

plex mode structure in Fig. 6 is a consequence of the mixed contribution to the period due to different barrier widths. We have observed clear periodicity in Fig. 6 for device D because it has two barriers in approximately 1:2 ratio, device E had several layers of $\sim 42 \text{ \AA}$ width, and similarly, device A has multiple 31 \AA barrier layers. We also note that a high barrier is not required to generate periodicity; any barrier that is purposely dominant would impose its effect. In device A₁, we purposely set the injection 41 \AA barrier to $x = 0.3$ and this has generated the confinement in Fig. 7 that corresponds to $L_{34}^{\text{A}_1} = 42.03 \text{ \AA}$. The Fourier transformation of data corresponding to device A₁ also shows a peak that corresponds to $L_{43}^{\text{A}_1} = 33.23 \text{ \AA}$, which is understandable as this device has five 31 \AA barriers in its layer sequence (more information can be found in the Appendix).

If wells have equal width, and all barriers widths are in a 1:2 ratio as in device I, we expect to obtain perfect periodicity. This can be observed in Fig. 7, where the periodicity corresponds to the layer width $L_{24}^{\text{I}} = 20.68 \text{ \AA}$, and the Fourier transform shows peaks also with 12 and 6 mode periods due to the symmetry of the device. If all barriers have equal width, perfect periodicity is attainable even when there is no significant difference in acoustic velocity in wells and barriers, as is the case in device J. The two well widths affect the phase of the observed oscillation, while the 20 \AA barrier causes confinement every 34 modes, which corresponds to $L_{34}^{\text{J}} = 20.35 \text{ \AA}$ when applying the approximation in Eq. (13).

We note that the lack of periodicity in the parabolic superlattices in devices F and G can be understood by Eq. (13) as well. The parabolic profiles of these devices were generated on a spatial resolution of monolayer thickness in GaAs, 2.825 \AA , and thus, regardless of the acoustic velocity that would correspond to each spatial segment, the resulting period in consecutive mode profile would be too large to be observed. There is also no dominant barrier layer, as these devices have a diffuse distribution of Al content in their layer sequence. This also raises an interesting effect with imperfect growth and tolerance. The rectangular heterostructure profiles in superlattice material systems may in reality undergo an

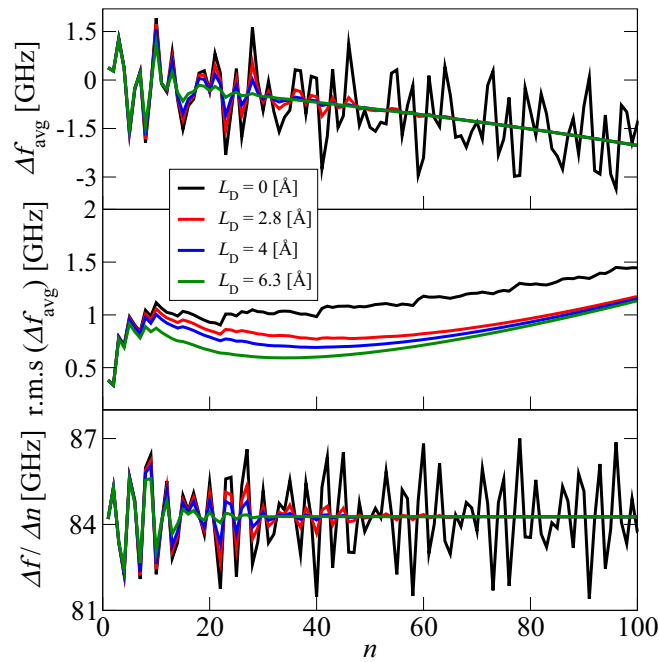


FIG. 8. We analyze structure D for several values of diffusion length using the annealing model in [40]. Top and middle: Frequency offset from the average approximation [Eq. (11)] and its cumulative root-mean-square average, respectively. Bottom: The frequency difference between consecutive resonant modes.

interdiffusion process that results in diffuse profiles for the superlattice interfaces. These effects are estimated to have up to 15 Å diffusion lengths [40–44]. In Fig. 8 we model growth tolerances in structure D using an annealing approach [40] by assuming a constant diffusion profile across the superlattice. We find that the observed periodicity in Fig. 7 vanishes for modes with a higher index and larger diffusion lengths. This also results in a smoother dependence of the frequency offset from the average approximation [Eq. (11)] resulting in a smaller rms average.

The effect in Fig. 7 can be controlled and manipulated through superlattice design, and this observation opens multiple engineering opportunities. Furthermore, the observed periodicity cannot be seen in the approximate approaches in Eqs. (3) and (10), and only the numerical consideration of Eq. (2) can explain the effect. The fine-tuning control of frequency is a fundamental trait in optical devices, thus the ability to perform analogous control of different acoustic resonant frequencies through superlattice design could find an important use in phononic applications. Conversely, our analysis shows that the thickness of layers within a superlattice could be inferred through precise measurements of the acoustic mode spacing, in analogy with x-ray diffraction measurements of crystalline solids.

V. TRANSPORT EFFECTS

In our previous work [28], we showed that optically generated picosecond acoustic (strain) pulses propagating along the growth direction of a QCL alter the band-structure potential sequentially and perturb the resonant tunneling between adjacent QCL periods. Here, we will examine the potential

THz QCL transport effects that could be induced by *resonant* (nonpropagating) acoustic phonon modes.

The transport in THz QCLs requires the use of models that include coherent effects, such as nonequilibrium Green function (NEGF) [45–47] or density matrix (DM) approaches [30,31,48–50], or the Wigner function formalism [51]. The NEGF approaches provide highly detailed results at a high numerical cost, whereas the DM approaches offer comparable outputs [48] with high numerical efficiency. The DM models deviate from NEGF simulations when high electric field bias is applied, making them less suitable for modeling midinfrared QCLs, however they are ideal for device optimization of THz QCL structures [29].

As such, we employ a density-matrix model [30,31] for calculation of electron transport in arbitrary THz QCLs. This model uses a tight-binding approximation for electronic structure calculation, which is then extended to an infinite period consideration of the QCL within the first-neighbor approximation. In the transport model, we treat various nonradiative interactions of electrons with alloy disorder (AD), longitudinal optical (LO) phonons, acoustic (AC) phonons, ionized impurities (II), interface roughness (IFR), and other electrons (EE).

To model the resonant acoustic effect, we add a static deformation potential $V_{S_n}(z)$ to the Hamiltonian for an electron in the QCL, which we assume to be directly proportional to the envelope of the local acoustic strain, $p_n(z)$. The BZE and BZC solutions of Eq. (2) provide standing-wave-like resonant modes with envelopes $p_n(z)$, giving

$$V_{S_n}(z) = M p_n(z), \quad (14)$$

where M is a modulation strength constant. For the acoustic signal generated in [28], we estimated that the strain amplitude perturbed the conduction-band potential by ~ 2 meV. With this assumption in Eq. (14), we can explore which acoustic modes affect electron transport, how the effects scale with modulation strength M , and which type of QCL designs are affected most significantly. We will dedicate special focus either to modes with frequencies ~ 100 GHz, as these have been reported experimentally in the modulation of superlattice band structures [11,13,15], or to 500–700 GHz modes, as a coherent phononic source has been reported in this range [52].

It is important to note that the strain standing wave, and hence deformation potential, oscillates in the time-domain around the zero point. The acoustic frequencies considered in this work are on the scale of a few hundred GHz, and the deformation, therefore, oscillates on a similar timescale to the electron dynamics within intersubband devices. As such, the deformation cannot be “averaged out” as a fast background effect, and a computationally demanding time-dependent model would be required for an accurate analysis of the acoustic effect on electron transport. In this work, however, we use a simplified time-independent approximation. Here, we consider the strain wave at its zero-phase point in the time domain, i.e., with the local deformation “frozen” at its maximum value. This allows us to gain insight rapidly into the effect of the spatial component of the acoustic deformation upon carrier dynamics.

In Fig. 9, we present the conduction-band potential of device A, as described in Sec. III and Ref. [28], where the

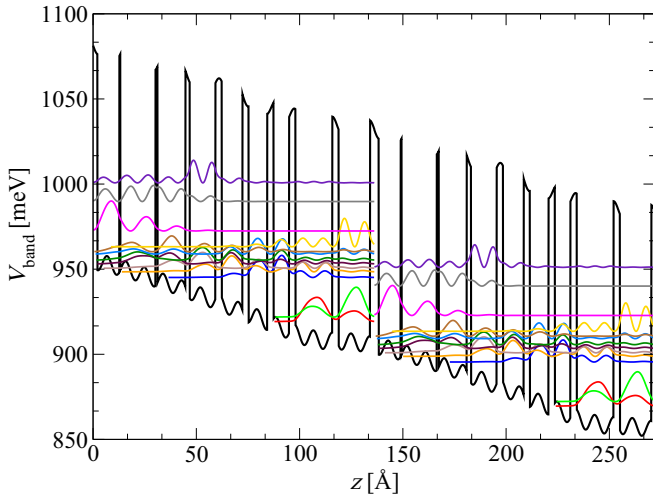


FIG. 9. Conduction-band potential of a hybrid QCL design [28] with the addition of the 30th acoustic mode with modulation $M = 5$ meV. Two periods are shown at the resonance bias $K = 3.63$ kV cm $^{-1}$ along with the corresponding wave-function moduli squared.

30th acoustic mode is added as strain to the original potential with modulation strength $M = 5$ meV to illustrate the effect of Eq. (14) on the band-structure potential. The potential itself is the main input for our Schrödinger-Poisson solver, from which we obtain the quasi-bound-state energies and the corresponding wave functions. This algorithm is coupled with a density matrix transport model, and we can obtain the dependence of the QCL emission frequency, f , current density J , and material gain g as a function of the applied electric field K . The K and J values directly correspond to the voltage and current in experimental device characterization, while the material gain offers insight into whether the structure lases or not, as well as providing information on the dynamic range. If a double-metal plasmonic waveguide is assumed, typical losses are ~ 20 cm $^{-1}$. Our simulations are reliable up to the peak of current density $J(K)$. Beyond this, the device enters a negative-differential-resistance (NDR) regime, and it becomes electrically bistable.

Our approach to understanding the effect of acoustic resonances on QCL performance is to analyze key QCL performance parameters derived from $g(K)$, $J(K)$, and $f(K)$, when (a) the modulation strength of a given mode is varied, and when (b) the mode index is varied, with a constant modulation strength.

In Fig. 10, we show the contribution of the first acoustic phonon mode with resonant frequency 17.4 GHz and modulation strengths M up to 5 meV in device A. The traces corresponding to $M = 0$ represent the unperturbed simulation outputs of our model. We observe a monotonically rising current density profile, material gain that surpasses the losses, and in the inset we note that this structure operates around 2.5 – 2.75 THz, which agrees very well with the experimental results [28]. There is a significant change in performance as the modulation strength M increases, where the most important effect is a shift of the current density peak, causing a reduction to the dynamic range.

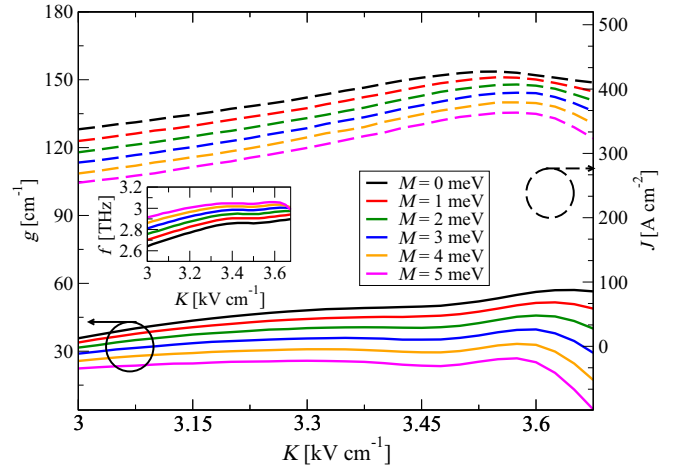


FIG. 10. Material gain and current density dependence on electric field when the first acoustic mode $n = 1$ is added with a range of modulation strengths to the conduction-band potential of device A.

To quantify the acoustic strain effect, we have extracted key performance parameters for the QCL—the dynamic range, peak gain, peak (NDR) current density, and the frequency of emission at the start of the NDR region—as a function of modulation strength, with results presented in Fig. 11 for the $n = 1, 2$, and 30 modes.

The material gain and the current density values in Figs. 11(a) and 11(b) are taken as the peak values of the corresponding traces in Fig. 10, whereas the frequency in Fig. 11(c) is taken at NDR point (peak of the current density in Fig. 10). The dynamic range in Fig. 11(d) is calculated as the current density difference between the NDR value and the value that corresponds to a material gain threshold of

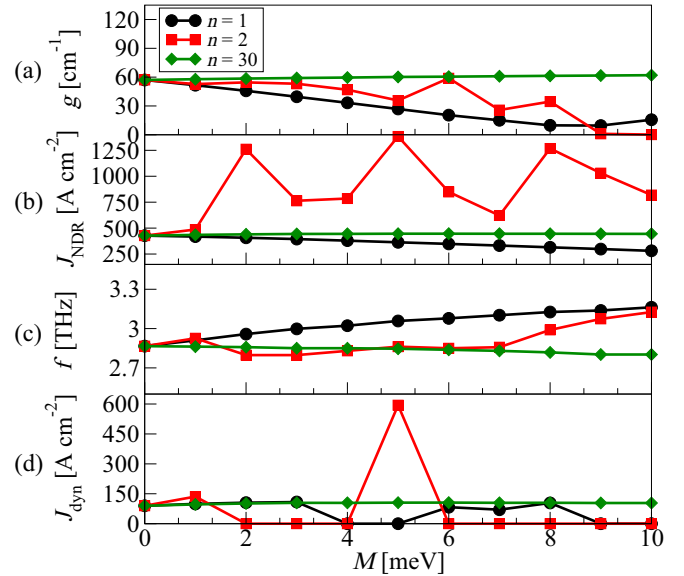


FIG. 11. Dependence of performance parameters for device A, as a function of modulation strength using acoustic modes $p_n(z)$ with indices $n = 1, 2, 30$. Results are shown for (a) peak gain, (b) current density at the NDR point, (c) emission frequency (at NDR point), and (d) dynamic range.

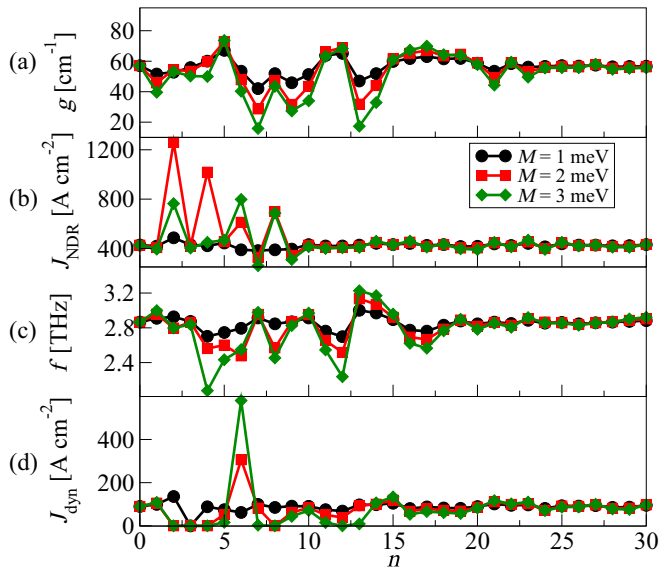


FIG. 12. Dependence of performance parameters for device A (hybrid QCL design), as a function of acoustic mode $p_n(z)$ index, using varying modulation strengths $M = 1, 2, 3$ meV. Results are shown for (a) peak gain, (b) current density at the NDR point, (c) emission frequency at NDR point, and (d) dynamic range. Values corresponding to $n = 0$ represent nonperturbed values (i.e., $M = 0$).

$\sim 20 \text{ cm}^{-1}$. We note that when the threshold bias is larger than the bias corresponding to the NDR value, the dynamic range is set to zero value, physically indicating a nonlasing structure. In Fig. 11(d), the second mode causes highly disruptive perturbation to the conduction-band potential leading to a nonlasing structure. This occurs because the second mode has a sinusoidal shape across one period, and when added to the conduction-band potential, as in Fig. 9, it causes abrupt changes in the shape of the conduction-band potential, drastically affecting QCL performance.

As expected, the perturbation to each of these values increases with respect to M . However, the effect of the higher-order $n = 30$ mode ($\sim 522 \text{ GHz}$) is shown to be considerably weaker than that of the lower modes.

This is confirmed further in Fig. 12, which shows that the variation in the QCL performance parameters oscillates and then decays as a function of acoustic mode index in all cases. The first 20 modes all affect transport, are capable of perturbing the conduction-band potential strongly, and even prevent the structure from lasing due to a strong shift of the NDR point and reduction of dynamic range. This is in agreement with previous reports of heterostructures being modulated by $\sim 100 \text{ GHz}$ acoustic pulses [11,13,15]. The lowest mode perturbs potential at its end points the most. In our simulations of transport, we always define the QCL period as starting (and ending) from the midpoint of the injection barrier. Adding a modulated standing wave $Mp_0(z)$ causes perturbation of the injection barrier so strongly affecting the tunneling. We note that this effect is significant in Fig. 11 even for low modulation strengths. However, higher-order modes have a negligible effect. This is explained by the periodicity of the high-order acoustic modes becoming much shorter than that of the QCL potential profile. As such, these act

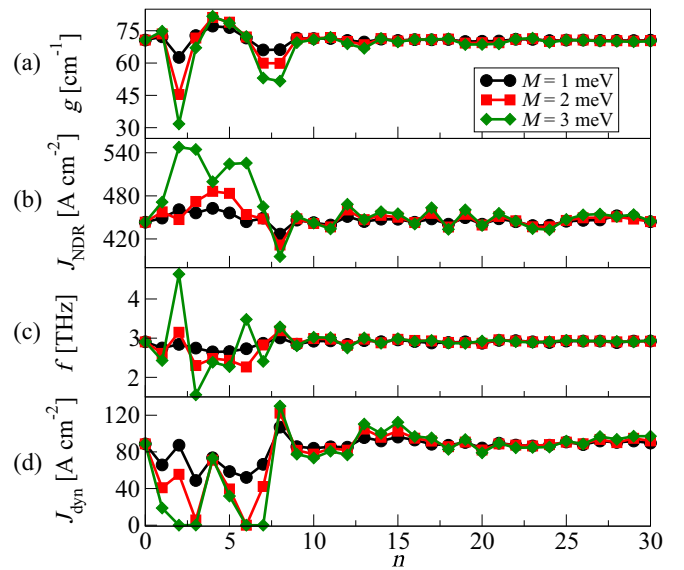


FIG. 13. Dependence of performance parameters for device B (LO phonon design), as a function of acoustic mode $p_n(z)$ index, using varying modulation strengths $M = 1, 2, 3$ meV. Results are shown for (a) peak gain, (b) current density at the NDR point, (c) emission frequency (at NDR point), and (d) dynamic range.

as a very high-frequency oscillation superimposed upon the QCL potential, which by analogy with the envelope-function model, will have only a weak effect on the eigenstates of the electrons.

In Figs. 13 and 14, we show comparable analyses of an LO-phonon depopulated QCL (device B) [10] and a BTC QCL (device C) [30], respectively. In both cases, we observe a similar general behavior to that in Fig. 11, however device

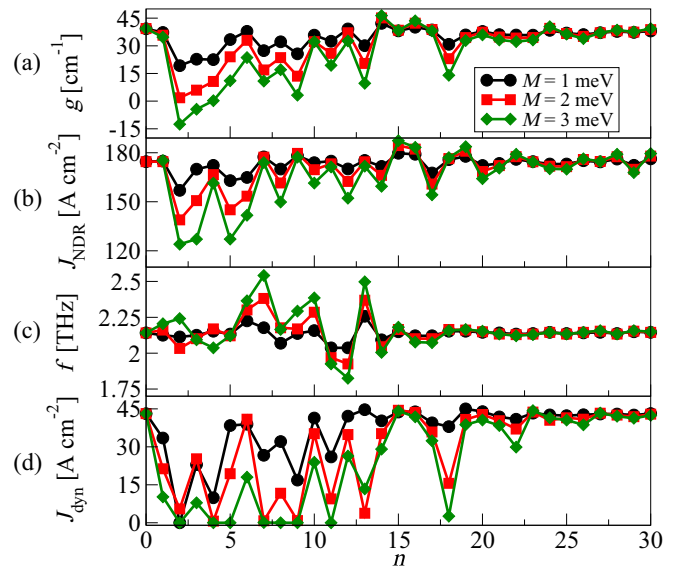


FIG. 14. Dependence of performance parameters for device C (BTC design), as a function of acoustic mode $p_n(z)$ index, using varying modulation strengths $M = 1, 2, 3$ meV. Results are shown for (a) peak gain, (b) current density at the NDR point, (c) emission frequency (at NDR point), and (d) dynamic range.

B displays very high sensitivity to the second acoustic mode. This is understandable, as the LO-phonon-depopulated QCL design is more sensitive to perturbations in the injection barrier, because the coupling between adjacent periods is more selective than in BTC and hybrid structures. Interestingly, the second mode causes very sudden deterioration of the material gain in Fig. 14, and this is likely due to the nature of the band-structure potential for this particular structure.

We note that both hybrid and LO-phonon-depopulated QCLs use similar resonant tunneling injection between adjacent periods, while BTC structures employ closely spaced minibands of states to depopulate the lower lasing level. For this reason, device C is more sensitive to lower mode perturbation.

As with device A, the acoustic perturbation effect oscillates and then decays at higher mode indices. In each case, the periodicity of the acoustic deformation potential becomes short compared with that of the QCL layer structure. LO phonon QCLs employ fewer quantum wells per period than BTC or hybrid designs, and they are therefore much shorter. As such, in Figs. 14 and 12, the added strain perturbs transport up to the 20th–24th mode, while in Fig. 13, the transport features saturate around the 10th mode. Interestingly, however, the frequency of the saturation point is comparable for all three designs (~ 400 GHz), as the LO phonon design has a wider separation between modes.

Modulation of the QCL emission frequency (on the scale of a few hundred GHz) is shown also to be possible for each of the three devices. This reaffirms our conclusion that acoustic modulation of QCL performance is caused by perturbing the conduction-band potential in the injection barrier. Thus, tunneling current and injection will be affected most strongly, though optical transitions, which typically happen in the first two wells of QCL period, are also likely to suffer some detuning due to applied strain. In all cases, we observe an oscillation in emission frequency (and current and gain) as the acoustic mode index increases. This occurs as lower modes have a spatial distribution that locally perturbs the potential profile in wells where the optical transition takes place.

VI. CONCLUSION

We have presented an analysis of acoustic resonances in arbitrary superlattice heterostructures, focusing on THz QCL devices. The model presented in Sec. II provides a flexible method to determine the resonant frequencies with high precision in arbitrary superlattice profiles. In Sec. IV, we discussed the precision of quasianalytical approaches, and we calculated the deviation from bulk and average approximations given in Eq. (11). We showed that a coarse approximation to the acoustic mode frequencies may be determined analytically from the period length and average acoustic velocity in the superlattice. However, approximately 2 GHz detuning of the acoustic mode spacing arises from the precise layer composition in the structure, and this may only be computed using numerical methods.

We show that this detuning effect is greatest in superlattices with high variation of acoustic velocity between layers. This is in some cases periodic, and its period is determined by resonances of the acoustic wave within barrier layers in the

structure. As such, this effect can be manipulated through superlattice layer design, and it offers another degree of freedom for fine-tuning frequency control of phononic devices.

In Sec. V we examined the effect of acoustic modes on electron transport in THz QCLs, using a deformation-potential approach. We found that the gain, threshold current, and emission frequency are all perturbed significantly for acoustic modes up to ~ 200 GHz, in line with previous experimental investigations. These affect the band-structure potential in its most sensitive location—the injection barrier, thus directly affecting resonant tunneling that couples carriers between adjacent periods, while slightly higher modes may also perturb band-structure potential in wells in which key optical transitions take place. For high-frequency modes, however, the acoustic deformation potential oscillates on a lengthscale much smaller than the QCL layer structure, and hence it has a negligible effect on transport. We also observed that overall, designs with longer period length display slightly higher sensitivity to acoustic perturbations.

This investigation demonstrates the potential for the design of THz QCLs for high-speed modulation, or higher-temperature operation, through the engineering of phonon interactions.

The data associated with this paper are openly available from the University of Leeds Data Repository [53].

ACKNOWLEDGMENTS

This work was supported financially by the Engineering and Physical Sciences Research Council (EPSRC) UK (Grants No. EP/V004743/1, No. EP/V004751/1, No. EP/P021859/1, No. EP/W028921/1, and No. EP/W033054/1), and the Medical Research Council (MRC) UK (UK Research and Innovation, Future Leader Fellowship MR/S016929/1). This work was undertaken on ARC4, part of the High Performance Computing facilities at the University of Leeds, UK. For the purpose of open access, the author has applied a Creative Commons Attribution (CC BY) licence to any Author Accepted Manuscript version arising from this submission.

The author contributions are as follows: Aleksandar Demić: writing—original draft preparation (lead); investigation (lead); methodology (equal); software; visualization; data curation. Alexander Valavanis: writing—reviewing and editing (lead); investigation (supporting); conceptualization (equal); methodology (equal); supervision (equal); funding acquisition (supporting). James Bailey: investigation (supporting); Andrey Akimov: investigation (supporting); Paul Dean: funding acquisition (supporting). Lianhe Li: investigation (supporting). A. Giles Davies: funding acquisition (supporting); conceptualization (supporting). Edmund H. Linfield: funding acquisition (supporting); conceptualization (supporting). Paul Harrison: conceptualization (equal). Anthony Kent: conceptualization (equal); supervision (equal); funding acquisition (equal). John Cunningham: conceptualization (equal); project administration (lead); supervision (equal); writing—reviewing and editing (equal); funding acquisition (equal).

The authors have no conflicts to disclose.

TABLE I. Layer composition of considered structures in Sec. IV. Layer widths in bold text represent the barriers; each structure ends with the injection barrier layer, layers in red text have different value of Al molar content x as specified in the third column.

Structure	Layer thicknesses (Å)	Al composition in $\text{Al}_x\text{Ga}_{1-x}\text{As}$ layers
Device A	106/ 5 /170/ 10 /135/ 21 /124/ 31 /100/ 31 /90/ 31 /75/ 31 /178/ 31 /152/ 41	$x = 0.14$
Device B	110/ 18 /115/ 35 /94/ 39 /184/ 48	$x = 0.15$
Device C	144/ 10 /118/ 10 /144/ 24 /144/ 24 /132/ 30 /124/ 32 /120/ 44 /126/ 50	$x = 0.1$
Device D	76.4/ 17.5 /154.7/ 33.7	$x = 0.3$
Device E	82/ 46 /72/ 41 /160/ 43	$x = 0.15, x = 0.075$
Device F	$x(z) = \frac{4x_0}{d_{sl}^2} \left(z - \frac{d_{sl}}{2}\right)^2$	$d_{sl} = 3000 \text{ Å}, dz = 2.825 \text{ Å}, x_0 = 0.14$
Device G	$x(z) = \frac{4x_0}{d_{sl}^2} \left(z - \frac{d_{sl}}{2}\right)^2 [1 + 0.18 \times \frac{4x_0}{d_{sl}^2} \left(z - \frac{d_{sl}}{2}\right)^2]$	$d_{sl} = 620 \text{ Å}, dz = 2.825 \text{ Å}, x_0 = 0.42$
Device H	42/ 17 /20/ 17	$x = 1$
Device D ₁	76.4/ 35 /154.7/ 33.7	$x = 0.3$
Device C ₁	144/ 10 /118/ 10 /144/ 24 /144/ 24 /132/ 30 /124/ 32 /120/ 44 /126/ 50	$x = 0.1, x = 1$
Device C ₂	144/ 10 /118/ 10 /144/ 24 /144/ 24 /132/ 30 /124/ 32 /120/ 44 /126/ 50	$x = 0.1, x = 1$
Device A ₁	106/ 5 /170/ 10 /135/ 21 /124/ 31 /100/ 31 /90/ 31 /75/ 31 /178/ 31 /152/ 41	$x = 0.14, x = 0.3$
Device I	150/ 20 /150/ 40 /150/ 80	$x = 1$
Device J	100/ 20 /100/ 20 /200/ 20 /200/ 20	$x = 0.1$

APPENDIX: LAYER COMPOSITION OF DEVICES

The layer composition of structures used in Sec. IV are shown in Table I, along with functions used to generate parabolic profiles of devices F and G.

- [1] S. M. Rytov, Acoustical properties of a thinly laminated medium, *Akusticheskij Zhurnal* **2**, 71 (1956).
- [2] C. Colvard, R. Merlin, M. V. Klein, and A. C. Gossard, Observation of Folded Acoustic Phonons in a Semiconductor Superlattice, *Phys. Rev. Lett.* **45**, 298 (1980).
- [3] B. Jusserand and M. Cardona, Raman spectroscopy of vibrations in superlattices, *Light Scattering in Solids V: Superlattices and Other Microstructures*, edited by M. Cardona and G. Güntherodt (Springer, Berlin, Heidelberg, 1989), pp. 49–152.
- [4] M. Klein, Phonons in semiconductor superlattices, *IEEE J. Quantum Electron.* **22**, 1760 (1986).
- [5] J. Sapriel, J. C. Michel, J. C. Toledano, R. Vacher, J. Kervarec, and A. Regreny, Light scattering from vibrational modes in GaAs-Ga_{1-x}Al_xAs superlattices and related alloys, *Phys. Rev. B* **28**, 2007 (1983).
- [6] J. Sapriel, B. Djafari-Rouhani, and L. Dobrzynski, Vibrations in superlattices; application to GaAs-AlAs systems, *Surf. Sci.* **126**, 197 (1983).
- [7] C. Thomsen, H. T. Grahn, H. J. Maris, and J. Tauc, Surface generation and detection of phonons by picosecond light pulses, *Phys. Rev. B* **34**, 4129 (1986).
- [8] S. Tamura and J. P. Wolfe, Acoustic phonons in multiconstituent superlattices, *Phys. Rev. B* **38**, 5610 (1988).
- [9] A. Kent, N. Stanton, L. Challis, and M. Henini, Generation and propagation of monochromatic acoustic phonons in gallium arsenide, *Appl. Phys. Lett.* **81**, 3497 (2002).
- [10] A. Bruchhausen, J. Lloyd-Hughes, M. Hettich, R. Gebbs, M. Grossmann, O. Ristow, A. Bartels, M. Fischer, M. Beck, G. Scalari *et al.*, Investigation of coherent acoustic phonons in terahertz quantum cascade laser structures using femtosecond pump-probe spectroscopy, *J. Appl. Phys.* **112**, 033517 (2012).
- [11] E. S. K. Young, A. V. Akimov, M. Henini, L. Eaves, and A. J. Kent, Subterahertz Acoustical Pumping of Electronic Charge in a Resonant Tunneling Device, *Phys. Rev. Lett.* **108**, 226601 (2012).
- [12] C. L. Poyser, L. H. Li, R. P. Campion, A. V. Akimov, E. H. Linfield, A. G. Davies, J. E. Cunningham, and A. J. Kent, A high electron mobility phonotransistor, *Commun. Phys.* **1**, 59 (2018).
- [13] C. Brüggemann, A. Akimov, A. Scherbakov, M. Bombeck, C. Schneider, S. Höfling, A. Forchel, D. Yakovlev, and M. Bayer, Laser mode feeding by shaking quantum dots in a planar microcavity, *Nat. Photon.* **6**, 30 (2012).
- [14] R. Köhler, A. Tredicucci, F. Beltram, H. E. Beere, E. H. Linfield, A. G. Davies, D. A. Ritchie, R. C. Iotti, and F. Rossi, Terahertz semiconductor-heterostructure laser, *Nature (London)* **417**, 156 (2002).
- [15] R. Paiella, R. Martini, F. Capasso, C. Gmachl, H. Y. Hwang, D. L. Sivco, J. N. Baillargeon, A. Y. Cho, E. A. Whittaker, and H. Liu, High-frequency modulation without the relaxation oscillation resonance in quantum cascade lasers, *Appl. Phys. Lett.* **79**, 2526 (2001).
- [16] J. Hillbrand, A. M. Andrews, H. Detz, G. Strasser, and B. Schwarz, Coherent injection locking of quantum cascade laser frequency combs, *Nat. Photon.* **13**, 101 (2019).
- [17] S. Barbieri, M. Ravaro, P. Gellie, G. Santarelli, C. Manquest, C. Sirtori, S. P. Khanna, E. H. Linfield, and A. G. Davies, Coherent sampling of active mode-locked terahertz quantum cascade lasers and frequency synthesis, *Nat. Photon.* **5**, 306 (2011).
- [18] A. A. Danylov, T. M. Goyette, J. Waldman, M. J. Coulombe, A. J. Gatesman, R. H. Giles, W. D. Goodhue, X. Qian, and W. E. Nixon, Frequency stabilization of a single mode terahertz

- quantum cascade laser to the kilohertz level, *Opt. Express* **17**, 7525 (2009).
- [19] S. Barbieri, P. Gellie, G. Santarelli, L. Ding, W. Maineult, C. Sirtori, R. Colombelli, H. Beere, and D. Ritchie, Phase-locking of a 2.7-THz quantum cascade laser to a mode-locked erbium-doped fibre laser, *Nat. Photon.* **4**, 636 (2010).
- [20] R. Eichholz, H. Richter, M. Wienold, L. Schrottke, R. Hey, H. T. Grahn, and H.-W. Hübers, Frequency modulation spectroscopy with a THz quantum-cascade laser, *Opt. Express* **21**, 32199 (2013).
- [21] L. Consolino, A. Taschin, P. Bartolini, S. Bartalini, P. Cancio, A. Tredicucci, H. Beere, D. Ritchie, R. Torre, M. Vitiello *et al.*, Phase-locking to a free-space terahertz comb for metrological-grade terahertz lasers, *Nat. Commun.* **3**, 1040 (2012).
- [22] S. Bartalini, L. Consolino, P. Cancio, P. De Natale, P. Bartolini, A. Taschin, M. De Pas, H. Beere, D. Ritchie, M. S. Vitiello, and R. Torre, Frequency-Comb-Assisted Terahertz Quantum Cascade Laser Spectroscopy, *Phys. Rev. X* **4**, 021006 (2014).
- [23] T. Kleine-Ostmann and T. Nagatsuma, A review on terahertz communications research, *J. Infrared, Millimeter, Terahertz Waves* **32**, 143 (2011).
- [24] W. Maineult, L. Ding, P. Gellie, P. Filloux, C. Sirtori, S. Barbieri, T. Akalin, J.-F. Lampin, I. Sagnes, H. Beere *et al.*, Microwave modulation of terahertz quantum cascade lasers: a transmission-line approach, *Appl. Phys. Lett.* **96**, 021108 (2010).
- [25] P. Gellie, S. Barbieri, J.-F. Lampin, P. Filloux, C. Manquest, C. Sirtori, I. Sagnes, S. P. Khanna, E. H. Linfield, A. G. Davies *et al.*, Injection-locking of terahertz quantum cascade lasers up to 35 GHz using RF amplitude modulation, *Opt. Express* **18**, 20799 (2010).
- [26] G. Liang, X. Hu, X. Yu, Y. Shen, L. H. Li, A. G. Davies, E. H. Linfield, H. K. Liang, Y. Zhang, S. F. Yu *et al.*, Integrated terahertz graphene modulator with 100% modulation depth, *ACS Photon.* **2**, 1559 (2015).
- [27] F. P. Mezzapesa, L. L. Columbo, C. Rizza, M. Brambilla, A. Ciattoni, M. Dabbicco, M. S. Vitiello, and G. Scamarcio, Photogenerated metamaterials induce modulation of cw terahertz quantum cascade lasers, *Sci. Rep.* **5**, 16207 (2015).
- [28] A. Dunn, C. Poyser, P. Dean, A. Demić, A. Valavanis, D. Indjin, M. Salih, I. Kundu, L. Li, A. Akimov *et al.*, High-speed modulation of a terahertz quantum cascade laser by coherent acoustic phonon pulses, *Nat. Commun.* **11**, 835 (2020).
- [29] A. Demić, Z. Ikonić, P. Dean, and D. Indjin, Dual resonance phonon–photon–phonon terahertz quantum-cascade laser: physics of the electron transport and temperature performance optimization, *Opt. Express* **28**, 38788 (2020).
- [30] A. Demić, A. Grier, Z. Ikonić, A. Valavanis, C. A. Evans, R. Mohandas, L. Li, E. H. Linfield, A. G. Davies, and D. Indjin, Infinite-period density-matrix model for terahertz-frequency quantum cascade lasers, *IEEE Trans. Terahertz Sci. Technol.* **7**, 368 (2017).
- [31] A. Demić, Z. Ikonić, R. W. Kelsall, and D. Indjin, Density matrix superoperator for periodic quantum systems and its application to quantum cascade laser structures, *AIP Adv.* **9**, 095019 (2019).
- [32] P. Harrison and A. Valavanis, *Quantum Wells, Wires and Dots: Theoretical and Computational Physics of Semiconductor Nanostructures*, 4th ed. (Wiley, Chichester, 2016).
- [33] M. Wienold, L. Schrottke, M. Giehler, R. Hey, W. Anders, and H. Grahn, Low-voltage terahertz quantum-cascade lasers based on LO-phonon-assisted interminiband transitions, *Electron. Lett.* **45**, 1030 (2009).
- [34] A. Huynh, B. Perrin, and A. Lemaître, Semiconductor superlattices: A tool for terahertz acoustics, *Ultrasonics* **56**, 66 (2015).
- [35] G. Tas and H. J. Maris, Electron diffusion in metals studied by picosecond ultrasonics, *Phys. Rev. B* **49**, 15046 (1994).
- [36] A. Khalatpour, A. K. Paulsen, C. Deimert, Z. R. Wasilewski, and Q. Hu, High-power portable terahertz laser systems, *Nat. Photon.* **15**, 16 (2021).
- [37] A. Jiang, A. Matyas, K. Vijayraghavan, C. Jirauschek, Z. R. Wasilewski, and M. A. Belkin, Experimental investigation of terahertz quantum cascade laser with variable barrier heights, *J. Appl. Phys.* **115**, 163103 (2014).
- [38] J. Jo, M. Santos, M. Shayegan, Y. Suen, L. Engel, and A.-M. Lanzilotto, Novel superlattice in a selectively doped wide parabolic quantum well with a modulated potential, *Appl. Phys. Lett.* **57**, 2130 (1990).
- [39] R. Reeder, A. Udal, E. Velmre, and P. Harrison, Numerical investigation of digitised parabolic quantum wells for terahertz AlGaAs/GaAs structures, in *2006 International Biennial Baltic Electronics Conference* (IEEE, Piscataway, NJ, 2006), pp. 1–4.
- [40] A. Valavanis, Z. Ikonić, and R. W. Kelsall, Intersubband carrier scattering in n- and p-Si/SiGe quantum wells with diffuse interfaces, *Phys. Rev. B* **77**, 075312 (2008).
- [41] B. Tuck, *Atomic Diffusion in III-V Semiconductors* (CRC Press, Boca Raton, 2021).
- [42] L. Wang, T.-T. Lin, M. Chen, K. Wang, and H. Hirayama, Terahertz quantum cascade laser considering compositional interdiffusion effect, *Appl. Phys. Express* **16**, 032007 (2023).
- [43] J. Roberts, R. Green, L. Wilson, E. Zibik, D. Revin, J. Cockburn, and R. Airey, Quantum cascade lasers grown by metalorganic vapor phase epitaxy, *Appl. Phys. Lett.* **82**, 4221 (2003).
- [44] X. Lü, E. Luna, L. Schrottke, K. Biermann, and H. Grahn, Determination of the interface parameter in terahertz quantum-cascade laser structures based on transmission electron microscopy, *Appl. Phys. Lett.* **113**, 172101 (2018).
- [45] T. Schmielau and M. Pereira Jr, Nonequilibrium many body theory for quantum transport in terahertz quantum cascade lasers, *Appl. Phys. Lett.* **95**, 231111 (2009).
- [46] V. Rindert, E. Önder, and A. Wacker, Analysis of High-Performing Terahertz Quantum Cascade Lasers, *Phys. Rev. Appl.* **18**, L041001 (2022).
- [47] D. O. Winge, M. Franckić, and A. Wacker, Simulating terahertz quantum cascade lasers: Trends from samples from different labs, *J. Appl. Phys.* **120**, 114302 (2016).
- [48] M. Lindskog, J. Wolf, V. Trinite, V. Liverini, J. Faist, G. Maisons, M. Carras, R. Aidam, R. Ostendorf, and A. Wacker, Comparative analysis of quantum cascade laser modeling based on density matrices and non-equilibrium Green's functions, *Appl. Phys. Lett.* **105**, 103106 (2014).

- [49] S. Soleimanikahnoj, O. Jonasson, F. Karimi, and I. Knezevic, Numerically efficient density-matrix technique for modeling electronic transport in mid-infrared quantum cascade lasers, *J. Comput. Electron.* **20**, 280 (2021).
- [50] B. A. Burnett, A. Pan, C. O. Chui, and B. S. Williams, Robust density matrix simulation of terahertz quantum cascade lasers, *IEEE Trans. Terahertz Sci. Technol.* **8**, 492 (2018).
- [51] O. Jonasson and I. Knezevic, Dissipative transport in superlattices within the Wigner function formalism, *J. Comput. Electron.* **14**, 879 (2015).
- [52] R. P. Beardsley, A. V. Akimov, M. Henini, and A. J. Kent, Coherent Terahertz Sound Amplification and Spectral Line Narrowing in a Stark Ladder Superlattice, *Phys. Rev. Lett.* **104**, 085501 (2010).
- [53] <https://doi.org/10.5518/1301>.